Desalination and Water Treatment
www.deswater.com

doi: 10.5004/dwt.2021.26818

216 (2021) 34–46
March

Experimental investigation on the characteristics of pressure drop and air/vapor flow over horizontal tube bundle with water-spray falling film

Yun She[a,b], Wen Chan[a], Fucheng Chang[a], Kaikai Guo[a], Yousen Zhang[c], Huixiong Li[a,*]

[a]*State Key Laboratory of Multiphase Flow in Power Engineering, Xi'an Jiaotong University, Xi'an 710049, China, Tel. +86-130-2289-1256; emails: huixiong@mail.xjtu.edu.cn (H. Li), sheyun.peter@gmail.com (Y. She), chanwen@stu.xjtu.edu.cn (W. Chan), 1454504477@qq.com (F. Chang), kaixinguo1022@126.com (K. Guo)*
[b]*Department of Mechanical Engineering, Tokyo Institute of Technology, 2-12-1-I6-33, Ookayama, Meguroku, Tokyo 152-8550, Japan*
[c]*Shenhua Guohua (Beijing) Electric Power Research Institute Co., Ltd., Beijing 100025, China, email: zhangyousen@126.com*

Received 28 May 2020; Accepted 4 November 2020

ABSTRACT

The horizontal tube falling film evaporation technology is one of the most promising desalination methods owing to its various advantages. The pressure drop of vapor plays a pronounced role in evaporation efficiency in low-temperature multiple-effect desalination (LT-MED). In this study, an experimental test bench by using air in the horizontal direction across a tube bundle with a vertical downward falling film was designed, and the flow characteristics of vapor of a large-scale desalination plant were simulated. Falling film pressure drops (FFPDs) under different conditions of air-inlet velocity, water-spray density, heating flux, and tube column number were obtained and analyzed. The experimental results indicate that FFPD can quadratically increase with the rise in air velocity, linearly rise with increments of spray density, and rapidly grow with the cumulative increase in tube columns. However, heat flux presented a minimal effect on FFPD because of the predominant portion volume of airflow relative to that of evaporated vapor. On the basis of the dimensionless analysis and the least-square multiple regression, a brand-new fitting correlation was proposed to predict FFPD. The proposed method corresponded well with the experimental data within the deviation of ±15%. The correlation also estimated the inter-tube average vapor velocity to be within 5–20 m/s in the first-effect evaporator of field-scale LT-MED in engineering. The brand-new correlation can also provide a theoretical reference in engineering design that considers vapor velocity and flow resistance in LT-MED.

Keywords: Horizontal tube bundle; Falling film; Two-phase flow; Pressure drop; Thermal desalination

1. Introduction

As the current extreme shortage of global freshwater resources has severely restricted the economic development of countries or regions, the development of desalination technologies has become an imminent and inevitable choice for human beings to obtain freshwater resources [1,2]. Low-temperature multi-effect desalination (LT-MED), a seawater evaporation technology involving horizontal tube falling film evaporation, has been widely used in large-scale commercial desalination production owing to its particular advantages of low evaporation temperature (less than 70°C) [3], low heat transfer temperature difference (from 2°C to 3°C only) [4], low energy consumption, high heat transfer coefficient, low manufacturing cost, corrosion resistance [5], easy coupling with thermal, nuclear, or solar power plants [6–9], etc. Furthermore, fossil fuel-powered

* Corresponding author.

thermal plants inevitably discharge extremely high waste heat, thus causing huge energy loss. This method can potentially integrate waste heat utilization with LT-MED to reduce this thermal pollution into the environment [10,11]. The working process of LT-MED can be generally elucidated from Fig. 1. The blowout seawater in the orifices falling from the top-row tubes to the bottom-row tubes generate layered water films attached around the tube surface, then the water films on this tube surface absorb sufficient heat as evaporated sources (i.e., second vapor is produced outside the tubes) from the first vapor flowing inside the tubes (Fig. 1b). During this heat transfer process, a phase change also occurs inside each tube, that is, the first vapor is condensed as distilled water when its condensation heat is released. However, the continuous development of second vapor generated from the water films can accumulate and cross the horizontally falling film tube bundle, inevitably causing a falling film pressure drop (FFPD). After the second vapor flows out of the effect evaporator, the vapor will enter the next-effect evaporator similar to the transfer of the first vapor shown in Fig. 1a. A slight increase in FFPD can result in the non-negligible reduction of evaporation efficiency because of tiny heat-transferred temperature differences of 2°C–3°C in the LT-MED [4].

Thus far, most studies have focused on the pressure drops of single- or two-phase fluids that cross in parallel directions over tube bundles. By using a previously collated large-quantity experimental dataset, Zhukauskas [12] summarized a widely applicable prediction equation of pressure drop for single air in the horizontal direction across an aligned or staggered plain tube bundle. Ishak et al. [13] presented an experimental measurement of the pressure drop characteristics of airflow over a staggered flat tube bank and found that the pressure drops decreased with the increase in Reynolds number, which differed from the result of Zhukauskas [12]. Given the complicated interactions between two phases over tube bundles, no well-predicted formula has been proposed for such pressure drop until now. According to a previous report, Lockhart and Martinelli [14] were the first researcher to propose the fundamental prediction of the two-phase pressure drop based on a two-phase flow inside a tube. Since then, Chisholm [15] has proposed a comprehensive theoretical basis to predict the pressure drop of two-phase flows inside tubes, thus further contributing to the work of Lockhart and Martinelli [14]. Some researchers have suggested that the pressure drop of two phases over a tube bundle is governed by a void fraction, an extremely important parameter (Schrage et al. [16], Dowlati et al. [17], Xu et al. [18], Feenstra et al. [19], etc.). Consolini et al. [20] assessed several previous void fraction correlations by conducting a two-phase pressure drop measurement. Their result showed that the correlation presented by Feenstra et al. [19] could effectively predict the experimental data in the vertical crossflow on horizontal tube bundles. Other researchers focused on two-phase flow patterns between tube bundles as another important factor of pressure drop. Mitrovic [21] observed three of the most classic flow patterns (discrete droplets, liquid columns, and liquid sheets) by conducting a single-tube falling film experiment. Hu and Jacobi [22] developed transition criteria equations and defined a graphic flow regime map for the aforementioned three flow patterns. Grant and Chisholm [23] experimentally observed three distinct flow patterns (bubbly, slug, and spray flows) from crossflows in horizontal tube bundles. Subsequently, many other researchers, such as Ulbric and Mewes [24], Xu et al. [25], Kanizawa and Ribatski [26], and Mao and Hibiki [27], suggested the use pf comprehensive classifications of flow patterns and proposed well-predicted regime maps based on the work of Grant and Chisholm [23]. However, the abovementioned past studies only qualitatively illustrated the flow patterns on two-phase pressure drops, and they failed to incorporate a formula to predict pressure drop in flow patterns. With the wide application of thermal desalination, a special two-phase flow over horizontal tube bundles has gradually become a popular research topic. This special flow process involves vapor flows across horizontal tube bundles combined with the use of gravitational falling films, resulting in different mechanisms of pressure drops relative to the conventional two-phase flow. Consequently, Liu et al. [4] conducted an experiment on a steam flowing across a horizontal tube bundle combined with the use of a falling film and established a fitting formula to predict the pressure drop, in which the two effects of falling film on the Reynolds number and steam Reynolds number were determined. Gong et al. [28] employed numerical methods

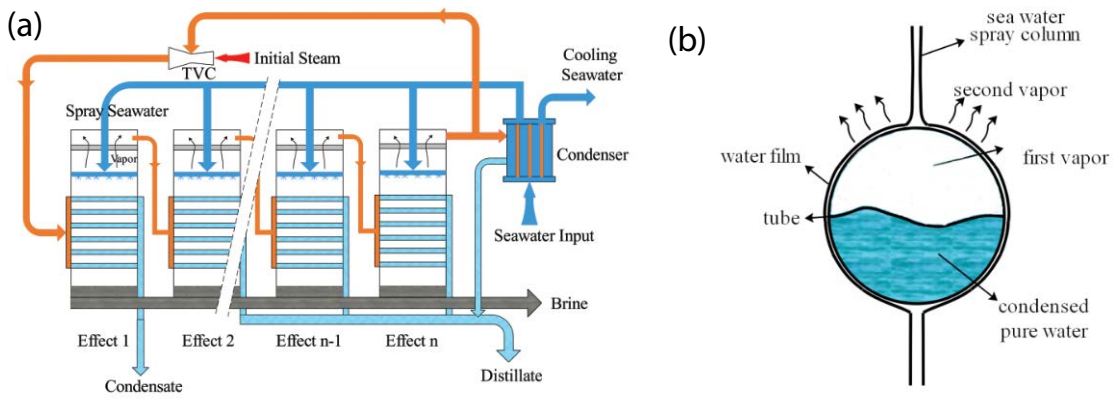

Fig. 1. Schematic diagram of the LT-MED: (a) steam flow of each effect in the LT-MED and (b) evaporation diagram in the single tube.

to analyze the distributions of a three-dimensional heat transfer coefficient based on the formula of Liu et al. [4] to verify the total pressure drop.

On the basis of aforementioned research, most studies have since focused on the traditional two-phase flow. In the recent literature review, scanty attention has been paid to the pressure drops of special two-phase flow cases that are extensively applied to thermal desalination areas. Although researchers have proposed fitting formulas based on their experimental dataset, the interactions between the two phases have been generally ignored. Notably, even a slight presence of FFPD in vacuum pressure evaporators can result in the non-negligible reduction of evaporation efficiency due to the small heat transfer temperature differences of 2°C–3°C. Therefore, a comprehensive method for calculating FFPD needs to be urgently developed. On the basis of the previous research, experimental measurement, and dimensionless analysis were combined in the present study to systematically investigate air/vapor flow and FFPD characteristics in a horizontal tube falling film evaporator to further enrich the theory of two-phase flow across a tube bundle with a falling film and provide a theoretical engineering design for LT-MED.

2. Experimental system and procedure

2.1. Experimental system and apparatus

The experimental system of air across a horizontal tube bundle with a vertical downward falling film is shown in Fig. 2. According to the different experimental processes, the experimental system is mainly composed of four component parts, namely, the air-providing system (AS), water-spray circulation loop (WCL), tube bundle system (TBS), and data acquisition system (DAS). The AS includes a centrifugal fan, an air heater, and a test section. The WCL includes water tank heater, a centrifugal pump, a water reheater, a high water tank, a water distributor, and a catchment basin. The TBS comprises 240 stainless heating rods arranged in a regular triangular tube bundle (Fig. 3) and controlled by an electrical power control panel. The DAS contains instruments, mainly for measuring temperature, flow rate, and pressure drop.

The test section used in this research is shown in Fig. 4. This core section consisted of three important parts, namely, the tube bundle zone, water distributor, and pressure drop measuring module. The horizontal tube bundle included 8 rows and 60 columns of stainless heating rods, with an outer diameter of 25.4 mm and a length of 500 mm. The top and bottom positions of the tube bundle were installed with non-heated half tubes (Fig. 3) to maintain the tube arrangement identical in case the air-flow field adjacent to the wall would be distorted. The maximum power capacity of each heating rod was 680 W.

The liquid distributor comprised a stainless water-spray plate and a transparent polycarbonate water-spray box that were connected by a flange and sealed by a silicone gasket. The water-spray plate was drilled evenly with 1,200 orifices, each one of them with a diameter of 2 mm. Fig. 5 shows the diagrammatic sketch of the water-spray plate. Three-layer distributive devices were installed inside the water-spray box to ensure that spray water would uniformly fall from above the tube rows.

The pressure drops (Δp) were acquired by observing the respective pressure sensors under the different conditions of air-inlet velocity (V_g), water-spray density (Γ), heating flux (q), and tube column number (N). The tube bundle was classified into seven groups for collecting data on the segmental pressure drop when the air would flush the tube bundle regardless of the presence or absence of falling water. The measuring positions are listed in Table 1. These measurement values correspond to the positions of mounted U-type manometers in view of ensuring reliable pressure drops to be acquired from the pressure sensors.

2.2. Experimental procedure

As mentioned in section 2.1 (Experimental system and apparatus), the experimental system was mainly composed

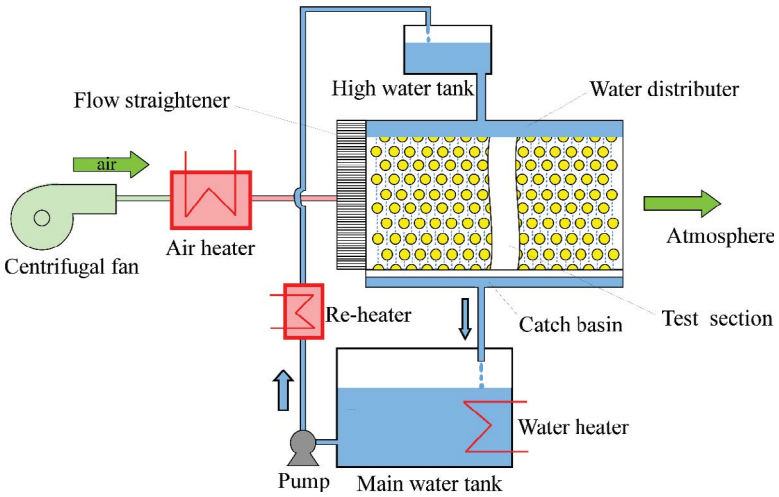

Fig. 2. Schematic diagram of the experimental system.

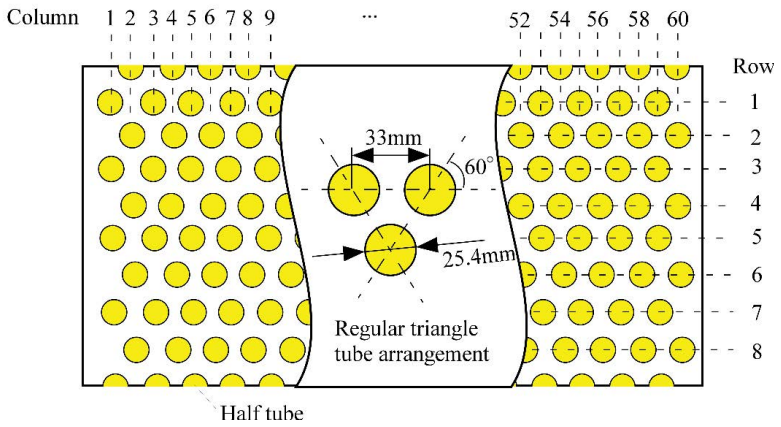

Fig. 3. Regular triangular tube bundle arrangement.

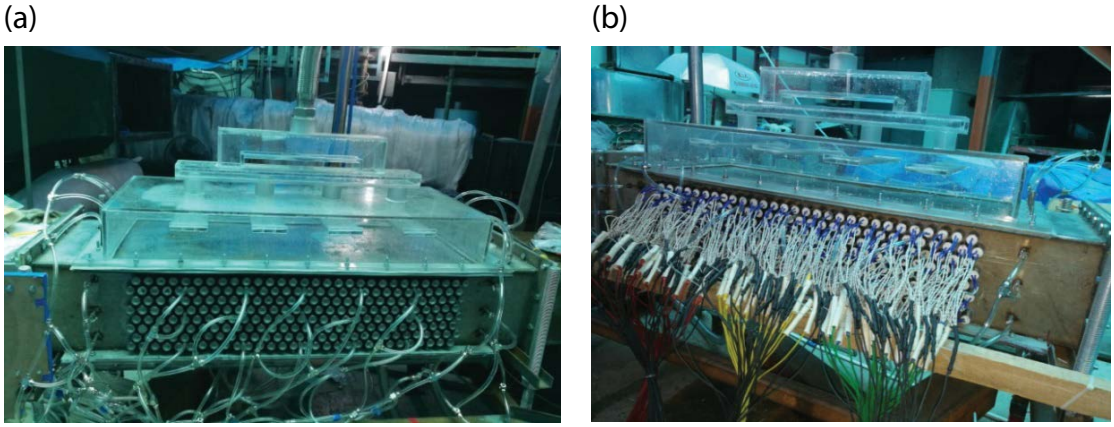

Fig. 4. Photograph of the test section: (a) front view and (b) rear view.

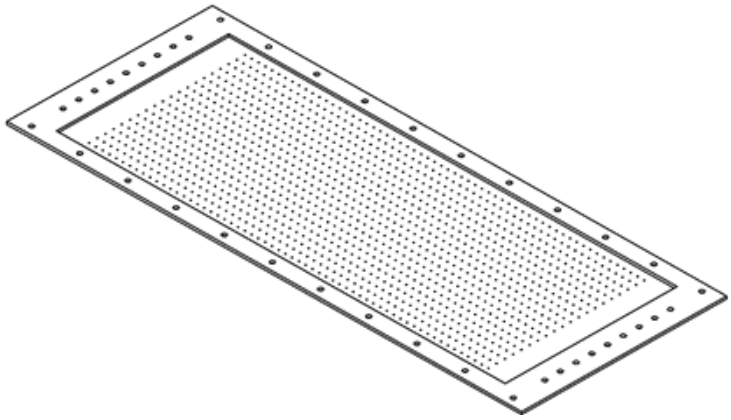

Fig. 5. Diagrammatic sketch of water-spray plate.

of four systems (AS, WCL, TBS, and DAS). The functions of each system are as follows:

2.2.1. Air-providing system

Air velocity ranging from 0.5 to 2.5 m/s was produced by a centrifugal fan and used to cross the horizontal tube bundle. The air-flown out of the tube bundle was directly driven into the ambient atmosphere. For the cold cases, the air heater was switched off to ensure that the air and water temperatures would be the same as the ambient temperature. For the hot cases, air was heated through the air heater from ambient temperature to water saturation temperature.

Table 1
Positions of pressure drop measurement parameters

Test groups	Pressure drop (Δp)	Test position (Col.)
0	Δp_{sum}	0–60
1	Δp_1	0–10
2	Δp_2	10–20
3	Δp_3	20–30
4	Δp_4	30–40
5	Δp_5	40–50
6	Δp_6	50–60

2.2.2. Water-spray circulation loop

For the hot cases, spray water was heated to saturation temperature by the main water tank heater. Saturated water was pumped from the main water tank into the high-water tank equipped with a water reheater to maintain the temperature of saturated water. After the saturated water was prepared, the control valve was opened to gravitationally inject spray water into the tube bundle at the spray density range of 0–0.10 kg/(m s). The spray volume was accurately monitored by an electric–magnetic flowmeter. The residual water that flowed out of the tube bundle was collected by a catchment basin; this residual water was automatically flowed back into the main water tank heater to complete the falling film circulation process. For the cold cases, the main water tank heater and the water reheater were switched off to ensure that the water temperature would be the same as the ambient temperature.

2.2.3. Tube bundle system

The TBS consisted of 240 stainless heating rods aligned as a regular triangle. For the hot cases, the TBS provided stable heat fluxes of 5, 10, and 15 kW/m^2 for the continuous evaporation of the liquid film. For the cold cases, each tube rod was switched off to maintain the tubular surface at room temperature.

2.2.4. Data acquisition system

The temperature, flow rate, and differential pressure sensors were calibrated prior the testing. The air velocity was measured by an L-type pitot tube with a measuring range of 0.049–1.6 kg/s. The water flow rate was measured by an electromagnetic flowmeter in the range of 0–32 m^3/h, then the spray density was calculated on the basis of the water flow rate. Total pressure drop was measured by a Rosemount differential pressure sensor with a measuring range of 0–2,480 Pa, while the segmental pressure drops were measured by another sensor group in the range of 0–500 Pa. The temperature was measured by an Omega T-type thermocouple in the range of −200°C to 400°C. The accuracy and position of each measuring device are shown in Table 2. Each parametric value was recorded by the Solarton IMP3595 system (Schlumberger Ltd., U.K.) equipped with a driver program written in C language. This system configuration could conveniently write and read experimental data and visualize such data on a computer screen. After the experimental system reached the stable operation state, each parameter was recorded for 50 s, that is, in 100 data points. Then, the effective experimental data were obtained by averaging the 100 points. The experimental data were collected until the two-phase flow and heat transfer reached the equilibrium condition, in which the total pressure drop values were finally monitored to be stable.

2.3. Experimental result and analysis

The effects of air-inlet velocity (V_g), water-spray density (Γ), heating flux (q), and tube column number (N) on the FFPD were determined. If no special denotation is cited in this research, then the FFPD (Δp_{sum}) is always defined as the pressure drop of airflow over the horizontal tube bundle with a water-spray falling film.

2.3.1. Effect of air velocity

The effect of V_g on the variation of Δp_{sum} when q = 0 and 5 kW/m^2 is shown in Fig. 6. Specifically, as depicted by Figs. 6a and b, the FFPD in the water-spray cases ($\Gamma \neq 0$ kg/(m s)) is much larger than that in the non-water spray cases (Γ = 0 kg/(m s)). By taking the smallest spray density (Γ = 0.02 kg/(m s)) for an example, when the air velocity was low (V_g = 0.5 m/s), the FFPD in Γ = 0.02 kg/(m s) was slightly larger than that in Γ = 0 kg/(m s). However, the FFPD difference between Γ = 0.02 kg/(m s) and Γ = 0 kg/(m s) increasingly widened with incremental V_g ranging from 0.5 to 2.5 m/s. Although a similar trend was observed in the water-spray cases, as indicated by Γ = 0.02 to 0.10 kg/(m s), the FFPD differences between the water-spray cases were not significant relative to those between the water-spray cases and non-water spray cases. As shown in Fig. 6a, it can also be seen that the FFPD value, as a quadratic function of air velocity, is aligned with the single-phase results obtained by

Table 2
Accuracies and positions of test instruments

Instrument	Type	Accuracy	Position
Thermocouple	T-type	±0.05°C	Water tank, spray box inlet, and air heater outlet
Flowmeter	E-mag C	±0.3%	Spray box inlet
Total differential pressure sensor	3051CD	±0.075%	Tube bundle (0–60 col.)
Sectional differential pressure sensor	YHT7085	±0.5%	Tube bundle (10 col. each)
Pitot tube	L-type	±0.5%	Fan outlet

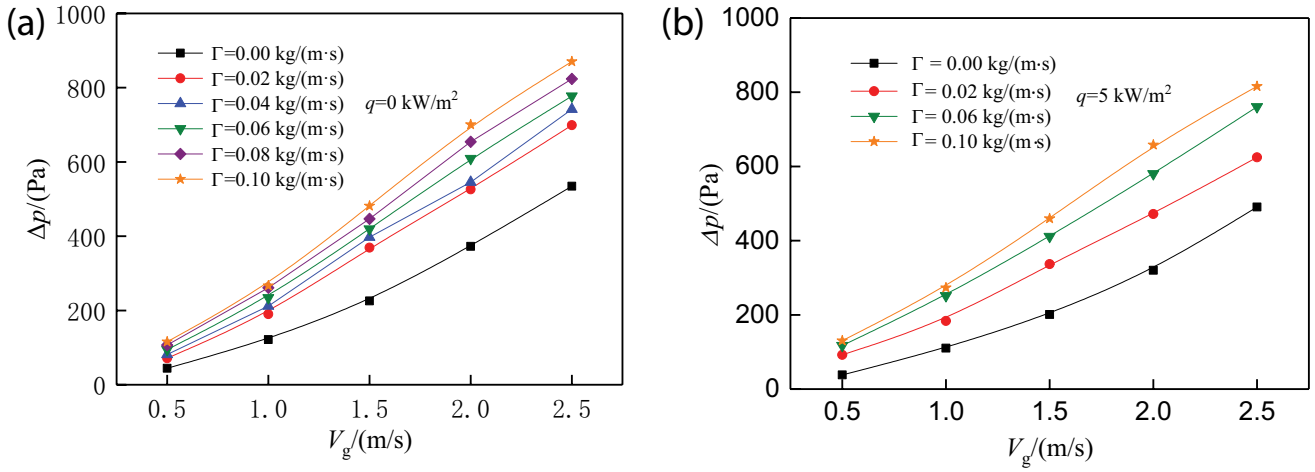

Fig. 6. FFPD as a function of air-inlet velocity in cold and hot states: Δp vs. V_g in (a) cold state and (b) hot state.

Zhukauskas [12]. The result of FFPD changes in the hot cases (q = 5 kW/m²) is plotted as a function of V_g in Fig. 6b. Similar to the trend of the cold cases, the FFPD variations among the different spray densities increasingly widened with the increase in V_g from 0.5 to 2.5 m/s. This trend also manifests the quadratic effect of air velocity on the FFPD values.

The possible mechanism of FFPD changes in the non-water spray cases and the water-spray cases mainly ascribes to two aspects. First, the effective airflow cross-sectional area is reduced after spray water falls on the tube surfaces. For example, the airflow area after the fall of water can decrease 1.13 times on the average relative to that of the non-water spray cases, leading to an increase in inter-tube air velocity. The FFPD can also expand 1.3 times larger as that of the non-water spray cases according to the quadratic effect on FFPD. Furthermore, interactions (splash, atomization, or collision) between water and air occurs through the tube bundle, a phenomenon closely associated with flow patterns. The turbulence extent should take the Lockhart–Martinelli number (X_{tt}) into account, which will be presented later in this paper. The other reason is that the water films attached around the tube surface represent the increase in diameter of each tube, thereby also increasing inter-tube air velocity. The decrease in film thickness (<0.55 mm) around the horizontal tube was reported previously by Hou et al. [29].

2.3.2. Effect of spray density

Fig. 7 illustrates FFPD as a function of spray density in the range of 0.02–0.10 kg/(m s). The FFPD shown in Fig. 7a has an almost linear function relative to the spray density of each velocity. Velocity influences the slope of the linear curve. Two reasons may explain the increasing trend in FFPD as a function of spray density. According to the literature regarding the single-tube experiment [21], the abovementioned phenomenon may be attributed to the transition of the falling film flow pattern when spray water falls from the upper tube to the next tube, and the flow patterns change from discrete droplets into liquid columns or turbulent liquid sheets with increments of spray density. In other words, the discrete drop mode, liquid column mode,

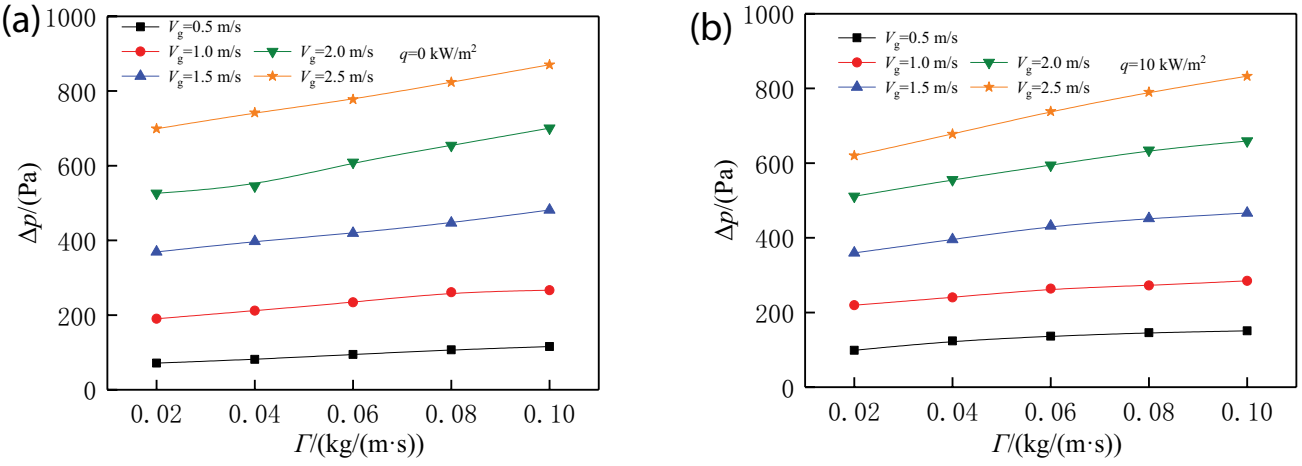

Fig. 7. FFPD as a function of spray density in cold and hot states: Δp vs. Γ in (a) cold state and (b) hot state.

and liquid sheet mode entail different flow areas in the cross-sectional tube bundle. For example, the droplet mode requires lesser airflow area than the column mode, while the column mode requires lesser airflow area than the liquid sheet mode. The liquid sheet pattern was not observed in our tube bundle experiment. Moreover, the column pattern persisted after the flow pattern transited from droplets to columns even though the spray density increased, that is, the diameters of the liquid column were nearly the same (average value: 2.3 mm) based on the preliminary experiment. Consequently, a new parameter, namely, the water fraction ($1-x$), was introduced in this research to explain the increase in FFPD in the column pattern. Water fraction is an effective factor of the Lockhart–Martinelli number (X_{tt}), as explained in section 3 (Mathematical model establishment of FFPD). The higher is the water fraction, the more turbulent are the interactions in the two-phase flow. Additionally, the increase in thickness of the water film affected the augmentation of FFPD in the form of increased diameter of the outer tube. Thus, the water film thickness was calculated using the fitting correlation [29], in which the average values were selected to be 0.27–0.37 mm at the spray density range of 0.02–0.10 kg/(m s). The increase in film thickness can increased the outer tube diameter to 25.94–26.14 mm relative to the initial tube diameter of 25.4 mm. As such, the water film thickness contributed to the FFPD at an increased ratio of 3.5%–4.8%.

The FFPD as a function of Γ in the hot cases is shown in Fig. 7b. The trend in the hot cases is similar to that in the cold cases. The differences in FFPDs between the cold and hot cases under the same velocity condition were not significant. The similarity may be explained by the mechanism in which the produced vapor volume is lesser than the airflow volume. Theoretically, the produced vapor and air will mix together and increase the mass flow rate of the air–vapor mixture. Thus, the effect on the FFPD with a mixture flow should be higher than the FFPD with an airflow only. However, the experimental results in this study contradicted the theoretical analysis. The evaporated vapor volume was estimated to be much lesser than the air volume. For example, the air mass flow rate at the lowest velocity of 0.5 m/s was 50 times different at the maximum relative to the vapor mass flow rate at the highest heat flux of 15 kW/m^2. Therefore, airflow as a factor has a predominant influence on FFPD.

2.3.3. Effect of heat flux

The FFPD as a function of heat flux (q) at the air velocities of 0.5 and 1 m/s are shown in Fig. 8. As illustrated in Fig. 8a, when the air velocity is low (V_g = 0.5 m/s), the FFPD continues to increase with the rise in heat flux. When the air velocity rises (V_g = 1.0 m/s), the FFPD slowly increases until it reaches the asymptotic state, as shown in Fig. 8b. As mentioned previously, air velocity plays a predominant role in FFPD relative to the evaporated vapor volume.

When the air-inlet velocity is low (i.e., the airflow rate is small), the generated vapor volume will increase the flow rate of the air–vapor mixture. As mentioned above, the mixture velocity has a quadratic effect on FFPD. Therefore, increasing the heat flux at a low air velocity can increase the FFPD. In contrast to the high air velocity, the air volume was much larger than the produced vapor volume in this study, a phenomenon that caused a dominant effect on the FFPD. Hence, we can reasonably conclude that when the air-inlet velocity continues to increase to a certain degree, the heat flux will have minimal impact on the FFPD.

2.3.4. Effect of tube columns

The cumulative pressure drop (Δp_i) as a function of incremental tube column (i) in the cold cases is given in Fig. 9. The cumulative pressure drop shown in Fig. 9a is a linear function of the tube columns under the non-water spray density condition. The cumulative pressure drop represents the accumulative airflow effect on the pressure drop as a function of tube columns. If each tube column is assumed to have the average pressure drop Δp_1, where $\Delta p_1 = \Delta p_{sum}/60$, then the 1–10 tube columns will have a pressure drop of Δp_1, the 1–20 columns will produce a pressure drop of $2\Delta p_1$, and the 1–60 columns will produce a pressure drop of $60\Delta p_1$. This trend indicates

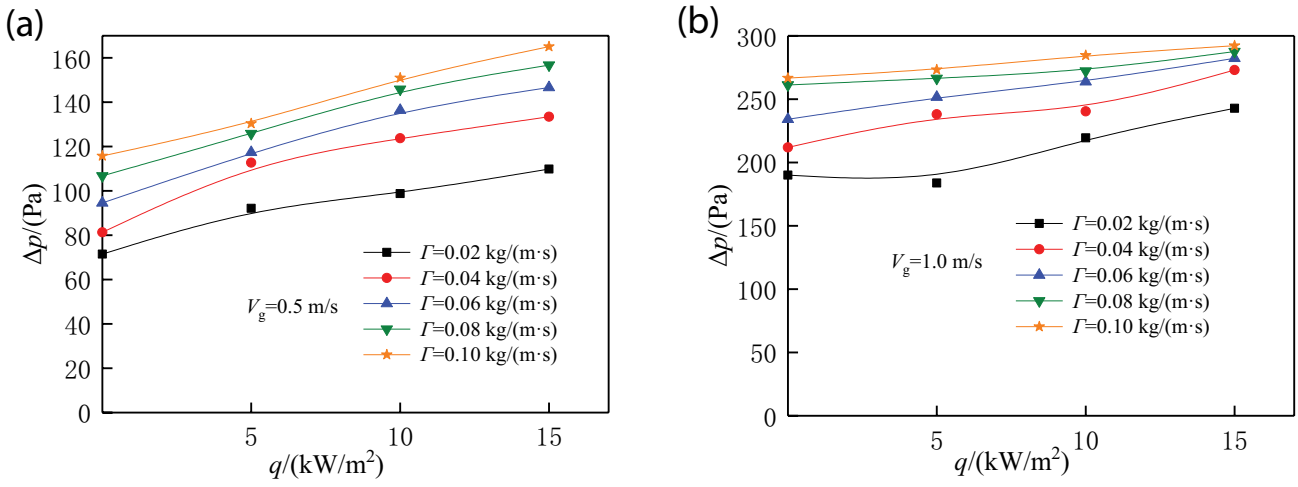

Fig. 8. FFPD as a function of heat flux at the air-inlet velocities of 0.5 and 1.0 m/s: Δp vs. q of (a) V_g = 0.5 m/s and (b) V_g = 1.0 m/s.

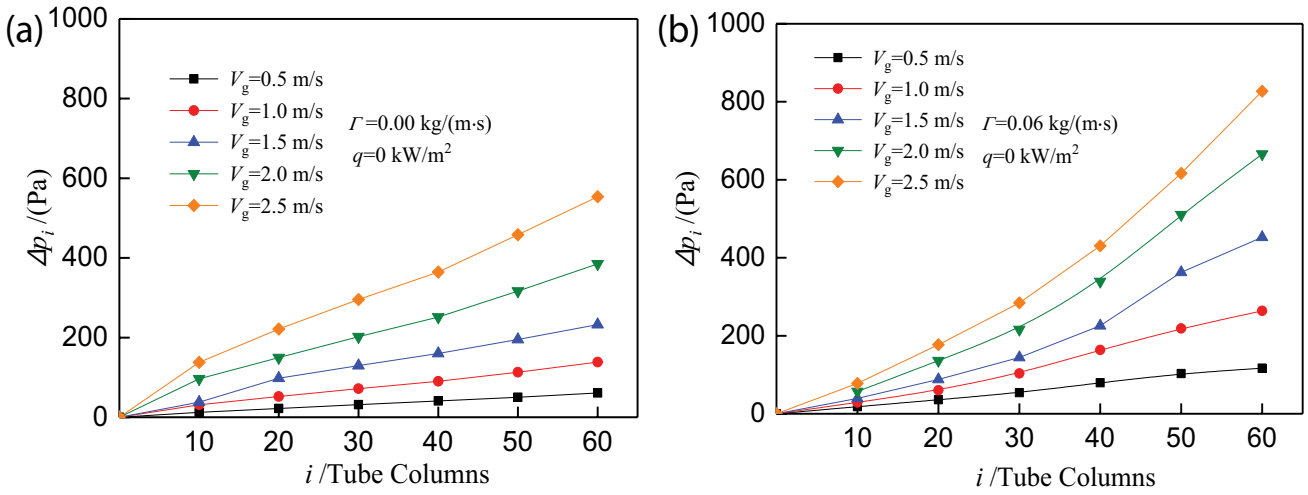

Fig. 9. Effect of tube columns in cold state: (a) non-water spray cases [Γ = 0 kg/(m s)] and (b) water-spray cases [Γ = 0.06 kg/(m s)].

that the cumulative pressure drop caused by each additional tube column is larger than that caused by the previous tube columns, further suggesting a cumulative effect on the pressure drop as a function of the tube columns. Furthermore, the cumulative effect exerted on the FFPD is linear, as suggested mathematically, which agrees well with the trend shown in Fig. 9a. However, as illustrated in Fig. 9b, the cumulative pressure drop in the water-spray cases rapidly rises with the increase in tube columns. This rapid increase can be explained from the standpoint of participating in falling water. The falling water can decrease the effective airflow area in each tube column, thereby increasing the airflow velocity between the tubes and pressure drop. For example, the airflow area after falling of water can decrease 1.13 times on the average relative to that of the non-water spray cases, leading to an increase in inter-tube air velocity by 1.13 times. Furthermore, the water film thickness also increases, which is equivalent to the increase in the outer diameter of each tube. This part increases the inter-tube air velocity by 1.03 times. As mentioned in section 2.3.1 (Effect of air velocity), the air-inlet velocity (V_g) has a parabolic effect on FFPD. The increased ratio of the FFPD can reach 32% in total relative to the non-water spray cases from a theoretical viewpoint. A cumulative effect can also be observed, that is, the cumulative pressure drop caused by each additional tube column is higher than that caused by the previous tube column when falling liquid is involved, thereby leading to a rapid increase in Δp_i.

For the cases in the hot state, the continuously generated vapor caused substantial fluctuations in the measurement of Δp_1 – Δp_6 (the details are not presented in this paper). Therefore, accurately determining the trend of Δp_i vs. i is a difficult endeavor. However, we can reasonably assume that the rapidly increasing trend will continue because of aforementioned minor influence of vapor with a high air velocity.

3. Mathematical model establishment of FFPD

A brand new fitting correlation for calculating Δp_{sum} is proposed on the basis of the experimental data. In view of simplifying the complexity of the two-phase flow, the Δp_{sum} calculation model is separated into two parts, namely, the pressure drop of an airflow across the tube bundle (Δp_{tb}) without spray water and that across the liquid columns (Δp_{col}). The former was proposed on the basis of the Blasius-type formula [30], while the latter was based on the dimensionless analysis method. In this manner, the influencing factor between the air and liquid phases can be comprehensively analyzed. The formula of Δp_{sum} is:

$$\Delta p_{sum} = \Delta p_{tb} + \Delta p_{col} \quad (1)$$

where Δp_{tb} and Δp_{col} represent the FFPD of an airflow across the tube bundle and across the liquid columns, respectively.

3.1. Basic assumption

As previously mentioned in section 2.3.1 (Effect of air velocity), Δp_{sum} is a quadratic function of inter-tube air velocity. However, air velocity is also influenced by other factors, such as tube arrangement, liquid column diameter, droplet splash, and atomization caused by the collision between spray water and tube surface, etc. Subsequently, reasonable assumptions should be generated to facilitate the theoretical calculation and expand the scope of application. The assumptions are as follows:

- The spray orifices have the same flow volume, and the liquid columns have the same diameter at each spray density.
- The liquid columns will not shift under the horizontal air flushes. The offset angle of the liquid columns is estimated to be 0.47°–11.57°, and their slight contributions to FFPD is estimated to range from 0.007% to 4% under the air-inlet velocity of 0.5–2.5 m/s.
- No droplet splash and atomization will occur between the tube surface and the liquid columns.
- The liquid film thickness around the tube surface is ignored.

3.2. Pressure drops of the tube bundle

Here, Δp_{tb} is the pressure drop produced by single-phase air in the horizontal direction across the tube bundle with a regular triangle arrangement. The past studies that have reported the calculation of this kind of pressure drop are summarized by Zhukauskas [12] as follows:

$$\Delta p_{tb} = 0.5 \cdot N \cdot \rho_g \cdot f_{tb} \cdot V_{g,act1}^2 \quad (2)$$

where $V_{g,act1}$ is the air actual velocity between tubes, N is the number of tube columns (N = 60), ρ_g is air density, and f_{tb} is the coefficient of pressure drop when air flows across tube bundle and defined as [30]:

$$f_{tb} = A \cdot \mathrm{Re}_{g1}^{B} \quad (3)$$

where A and B are constants, and Re_{g1} is a function of $V_{g,act1}$ and defined by:

$$\mathrm{Re}_{g1} = \frac{\rho_g \cdot V_{g,act1} \cdot D}{\mu_g} \quad (4)$$

where μ_g is dynamic viscosity of air, and D is diameter of each tube, $V_{g,act1}$ is calculated by the continuity equation of:

$$A_0 \cdot V_g = \left(A_0 - A_1\right) \cdot V_{g,act1} \quad (5)$$

where A_0 is cross-sectional area of the tube bundle, A_1 is the yellow area occupied by the tubes, $(A_0 - A_1)$ is the white area representing the air effective flow area (Fig. 10).

On the basis of the non-water spray experimental data, the fitting correlated formula for calculating the pressure drop of an airflow across the tube bundle is:

$$\Delta p_{tb} = 0.5 \cdot N \cdot \rho_g \cdot \left(41.37 \cdot \mathrm{Re}_{g1}^{-0.45551}\right) \cdot V_{g,act1}^2 \quad (6)$$

The deviation between the experimental data and calculated data are within ±1%, as shown in Fig. 11. The calculated data agree well with the experimental data.

3.3. Pressure drops of liquid columns

In view of simplifying the complexity of the two-phase flow, the liquid columns are regarded to be isodiametric circular cylinders. In this manner, the pressure drop of air across the liquid columns can be converted into that of an airflow across circular cylinders. Regarding the pressure drop of an airflow across the cylinder, Schlichting [31] summarizes the calculation formula as follows:

$$\Delta p_{col} = 0.5 \cdot N \cdot \rho_g \cdot C_d \cdot V_{g,act2}^{*\,2} \quad (7)$$

where C_d is the pressure drop coefficient of the circular cylinders, and $V_{g,act2}^{*}$ is the corrected air velocity between tubes with the presence of spray water.

3.3.1. Ideal air velocity between tubes

Figs. 10 and 12 are compared for analysis. The existing liquid columns have caused the airflow area to be further reduced. Thus, the continuity equation is again used to calculate the ideal air velocity between tubes:

$$A_0 \cdot V_g = \left(A_0 - A_1 - A_2\right) \cdot V_{g,act2} \quad (8)$$

where $V_{g,act2}$ represents the ideal air velocity between tubes with the presence of spray water, and A_2 is the sectional area occupied by the liquid columns.

Different spray densities entail different liquid column diameters (d). As shown by the preliminary experiment (Fig. 13), the diameter of each spray slightly decreases with an increase in the water-spray density. The quantitative diameters are listed in Table 3. As we can see, the diameters of the sprayed liquid column changed slightly. Thus, the average diameter (d_{cr} = 2.3 mm) was employed in the subsequent calculation.

3.3.2. Corrected air velocity between tubes

The ideal air velocity represents an ideal situation in which the influencing factors between the two phases are not considered. Therefore, the corrected velocity should be based on many factors, such as turbulence between the two

Fig. 10. Effective flow cross-sectional area at Γ = 0 kg/(m s). (a) front view and (b) sectional view.

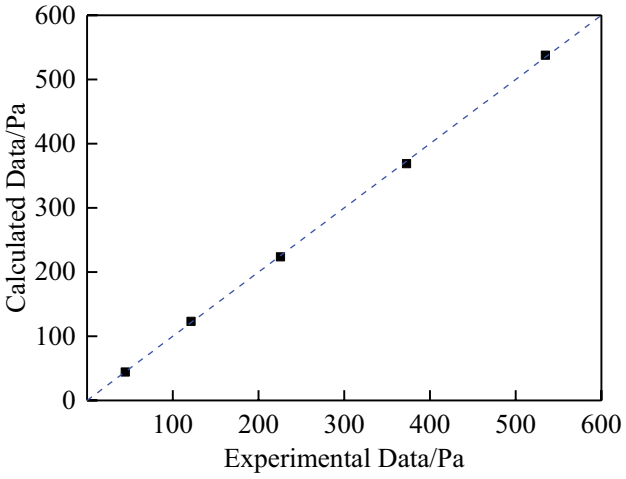

Fig. 11. Comparison between experimental and calculated values.

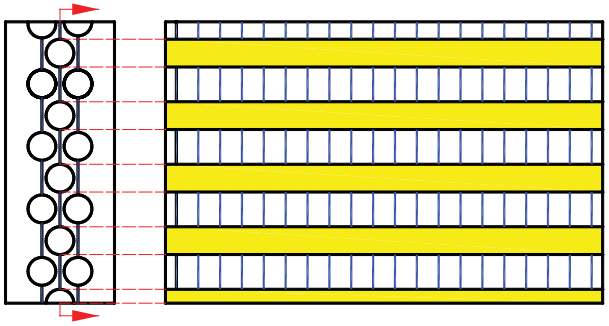

Fig. 12. Effective flow cross-sectional area at Γ ≠ 0 kg/(m s). (a) front view and (b) sectional view.

Table 3
Quantitative liquid column diameter values

Spray density, Γ (kg/m s)	Liquid column diameter, d (mm)
0.02	2.60
0.04	2.32
0.06	2.17
0.08	2.13
0.10	2.12

phases, fluid physical properties, and Reynolds number, etc. Each possible factor can be expressed as:

$$V^*_{g,\mathrm{act2}} = f\left(V_{g,\mathrm{act2}}, V_l, \rho_g, \rho_l, \mu_g, \mu_l, g, d, D, \frac{1-x}{x}\right) \tag{9}$$

where V_l is the water-spray velocity flown out of the orifices; ρ_g and ρ_l are air density and water density, respectively; μ_g and μ_l are air dynamic viscosity and water dynamic viscosity, respectively; and x is the air fraction inside tube bundle and defined as:

$$x = \frac{\rho_g \cdot V_g \cdot A_g}{\rho_g \cdot V_g \cdot A_g + \rho_l \cdot V_l \cdot A_l} \tag{10}$$

where A_g is the cross-sectional area of the tube bundle, and A_l is the circular area of 1,200 orifices.

Eq. (9) is further abbreviated as non-dimensional number based on the π principle. Consequently, Eq. (11) can be expressed as follows:

$$\frac{V^*_{g,\mathrm{act2}}}{V_{g,\mathrm{act2}}} = f\left(\mathrm{Fr}_g, \frac{\mathrm{Re}_l}{\mathrm{Re}_{g2}}, X_{\mathrm{tt}}\right) \tag{11}$$

where Fr_g is the Froude number, Re_l is the water Reynolds number, Re_{g2} is the air Reynolds number, and X_{tt} is the Lockhart–Martinelli number [14].

$$\mathrm{Fr}_g = \frac{g \cdot D}{V^2_{g,\mathrm{act2}}} \tag{12}$$

$$\mathrm{Re}_l = \frac{2 \cdot \Gamma}{\mu_l} \tag{13}$$

$$\mathrm{Re}_{g2} = \frac{\rho_g \cdot V_{g,\mathrm{act2}} \cdot D}{\mu_g} \tag{14}$$

$$X_{\mathrm{tt}} = \left(\frac{1-x}{x}\right)^{0.9} \cdot \left(\frac{\rho_g}{\rho_l}\right)^{0.5} \cdot \left(\frac{\mu_l}{\mu_g}\right)^{0.1} \tag{15}$$

Thus, Eq. (11) can be further expressed as:

$$\frac{V^*_{g,\mathrm{act2}}}{V_{g,\mathrm{act2}}} = a_0 + X^{a_1}_{\mathrm{tt}} \cdot \left(\frac{\mathrm{Re}_l}{\mathrm{Re}_{g2}}\right)^{a_2} \cdot \left(\mathrm{Fr}_g\right)^{a_3} \tag{16}$$

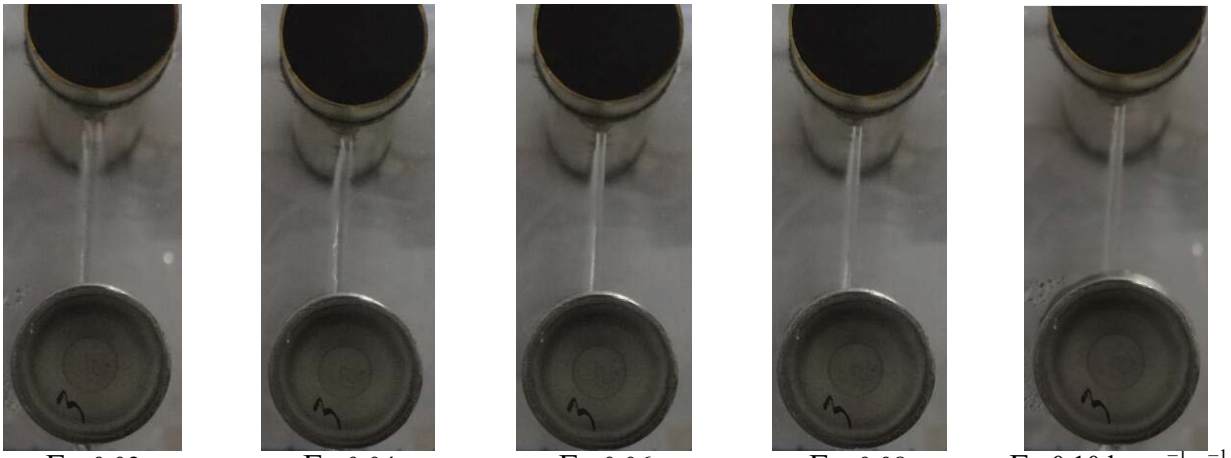

Fig. 13. Liquid column diameter with different spray densities.

By combining Eqs. (7) and (16), Δp_{col} can be expressed as:

$$\Delta p_{col} = 0.5 \cdot N \cdot C_d \cdot \rho_g \cdot V_{g,act2}^2 \left(a_0 + X_{tt}^{a_1} \cdot \left(\frac{Re_l}{Re_{g2}} \right)^{a_2} \cdot \left(Fr_g \right)^{a_3} \right)^2 \quad (17)$$

On the basis of the experimental data, regression analysis was employed to achieve the value of a_0, a_1, a_2, and a_3, which have the values of −1.44, 0.386, −0.336, and 0.00522, respectively.

3.4. Fitting correlation for the FFPD

Combining Eqs. (1), (5), (6), (8), and (17) yields the FFPD calculation formula of:

$$\Delta p_{sum} = 0.5 \cdot N \cdot \rho_g \cdot f_{sum} \cdot V_g^2 \quad (18)$$

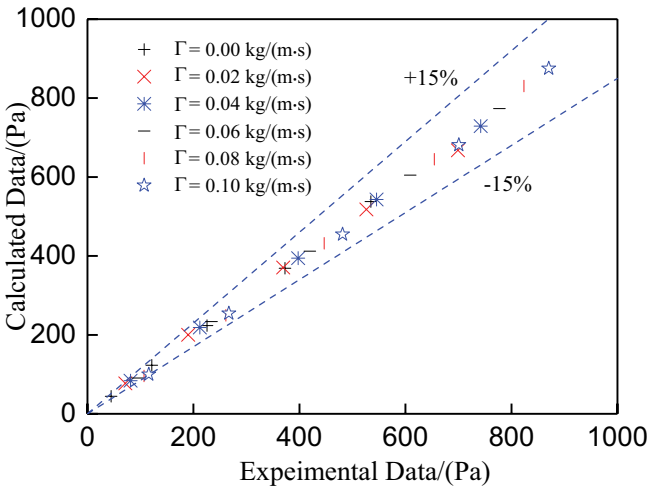

Fig. 14. Comparison between experimental and calculated values.

where

$$f_{sum} = 41.37 \cdot Re_{g1}^{-0.45551} + C_d \cdot \left(-2.929 + 2.034 \cdot X_{tt}^{0.386} \cdot \left(\frac{Re_1}{Re_{g2}} \right)^{-0.336} \cdot \left(Fr_g \right)^{0.00522} \right)^2 \quad (19)$$

where Re_{g1} = 1,570–7,850, Re_{g2} = 1,570–7,850, and Re_l = 30–200.

Eq. (19) can be used for dimensionless analysis, as it not only considers the influences of air Reynold number (Re_g) and water Reynold number (Re_l) but also the gas–liquid turbulence (X_{tt}) between air and water. The calculated result of FFPD is plotted in Fig. 14. The proposed correlation matches the experimental data at a deviation of ±15% for the spray density of Γ = 0–0.10 kg/(m s).

3.5. Vapor flow in the LT-MED evaporator

On the basis of the dimensionless analysis, a reasonable formula (Eq. (16)) for calculating the air actual velocity between tubes was adopted. Fig. 15a shows the calculation result of the proposed equation of the actual air velocity between tubes at the spray density of Γ = 0.02–0.10 kg/(m s). Thus, we transformed air velocity into vapor velocity at the pressure of p = 21.8 kPa, with the same vacuum environment as that in the first-effect evaporator in the LT-MED plant. As shown in Fig. 15b, the average vapor velocity between tubes in the tube bundle of the first-effect evaporator is in the range of 5–20 m/s at a spray density of 0.02–0.10 kg/(m s), corresponding to the same order of velocity magnitude numerically simulated in the LT-MED plant [28]. Furthermore, the inter-tube air velocity values first increase linearly and then further slow rise with the increase in air-inlet velocity for each spray density. The linear increase occurs at a lower air-inlet velocity of V_g = 0.5–1.5 m/s in which the shear force is unable to overcome the gravity forces [32]. Thus, the spray water column

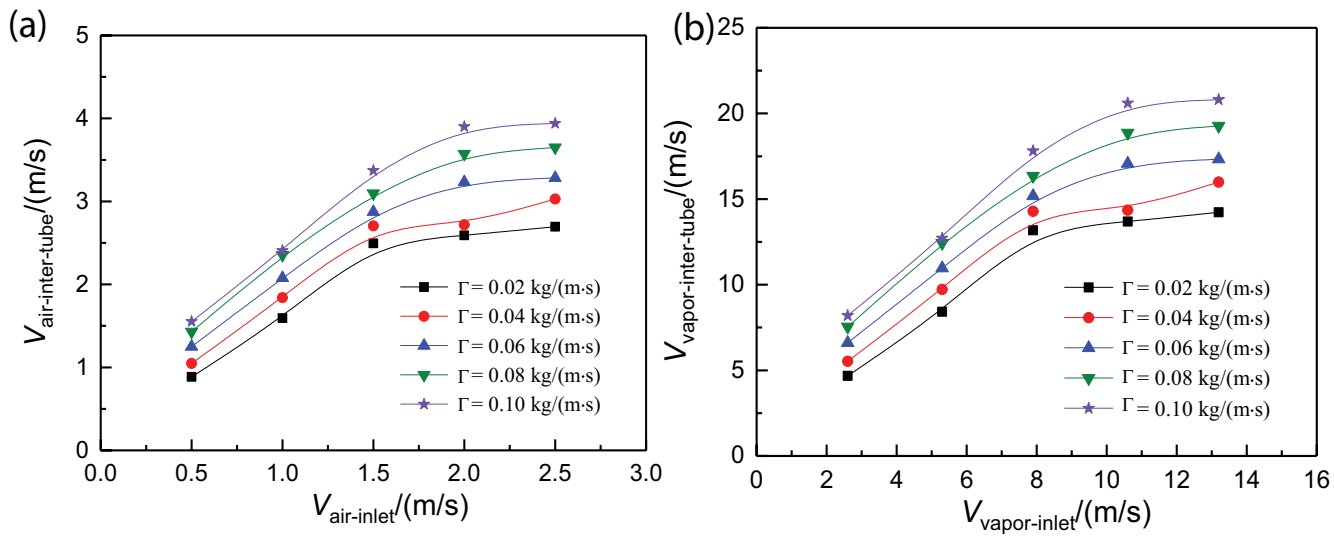

Fig. 15. Actual air/vapor velocity between tubes vs. air-inlet velocity of the test section. Actual inter-tube (a) air velocity and (b) vapor velocity

can keep the original liquid-column shape. As mentioned in the analysis of the spray–density effect, the effective airflow area is reduced due to the water phase also occupying certain areas. As a result, the inter-tube air velocity increases linearly with the rise in air-inlet velocity. The slow increase in inter-tube air velocity with the rise in air-inlet velocity can be explained from two distinct mechanisms. One mechanism ascribes to different flow patterns caused by the relatively high inter-tube velocity in the falling two-phase flow. In particular, when the air velocity exceeds 1.5 m/s, the shear force exceeds the gravity forces. The vertical falling film can transfer to a horizontal flow along the same direction of airflow, namely, the traditional two-phase flow. However, the interactions between the air and water phases are drastic, producing different two-phase flow patterns. Thus far, many studies have attempted to classify the traditional two-phase flow patterns, such as bubble, churn, intermittent, and annular patterns, etc., [24–27]. Mao and Hibiki [27] previously found flow pattern transitions to the churning or annular state when the air velocity was more than 1 m/s in the normal triangular tube bundle arrangement. We can speculate from the momentum conservation that the pattern will lower the air velocity and increase the water velocity. However, once the liquid columns become deformed due to the high air velocity, the effective airflow area increases relative to the low air-inlet velocity, thereby lowering the inter-tube velocity. These two reasons may explain the slow increase in inter-tube velocity.

4. Conclusions

This study comprehensively combined experiment and correlation to investigate the air/vapor flow and pressure drop characteristics over a horizontally falling film tube bundle. The main conclusions can be drawn as follows.

- FFPD increases quadratically with the increases in air velocity, rises linearly with increments of spray density, and rise rapidly with increase in tube columns. However, heat flux has a minimal effect on the FFPD because of the predominant portion of airflow volume relative to that of the evaporated vapor volume.
- The FFPD in water-spray cases is much larger than that in the non-water spray cases ($\Gamma = 0$ kg/(m s)) owing to the airflow cross-sectional area reduction after the falling of spray water in the tube bundle.
- A brand new correlation for predicting the FFPD is proposed on the basis of the dimensionless analysis and experiment data within the deviation of ±15%.
- The inter-tube average vapor velocity was estimated in the range of 5–20 m/s in the first effect of the LT-MED evaporator at the spray density of 0.02–0.10 kg/(m s), corresponding to the order of magnitude of engineering data. The inter-tube air velocity values first increase linearly and then slow rise with the increase in air-inlet velocity for each spray density.

Our study intended to prove the reasonable concept and principle of establishing the FFPD formula. The inter-tube air/vapor velocity was also estimated reasonably. In the future, related studies can employ particle image velocimetry (i.e., PIV approach) to directly measure and verify gaseous velocity between tubes. Additionally, the flow pattern classifications of falling film two-phase flow over a tube bundle can be regarded a key parameter in determining FFPD. The aforementioned proposals can thus be regarded a direction of further research.

Symbols

A_0	—	Cross-sectional area of tube bundle, m^2
A_1	—	Cross-sectional area occupied by tubes, m^2
A_2	—	Cross-sectional rea occupied by liquid columns, m^2
C_d	—	Pressure drop coefficient of circular cylinder
D	—	Tube diameter, m
Fr_g	—	Air Froude number
N	—	Tube column number
Re_{g1}	—	Air Reynolds number in non-water spray system
Re_{g2}	—	Air Reynolds number in spray system
Re_l	—	Spray Reynolds number
V_g	—	Air inlet velocity of test bench, m/s
$V_{g,\mathrm{act1}}$	—	Air actual velocity between tubes without spray water, m/s
$V_{g,\mathrm{act2}}$	—	Air actual velocity between tubes with spray water, m/s
$V^*_{g,\mathrm{act2}}$	—	Corrected air velocity between tubes with spray water, m/s
$V^*_{\mathrm{vap,act2}}$	—	Corrected vapor velocity between tubes with spray water, m/s
X_{tt}	—	Lockhart–Martinelli number
d	—	Liquid column diameter, m
f_{sum}	—	Total resistance coefficient over tube bundle
g	—	Gravitational acceleration, m/s^2
Δp_{sum}	—	Falling-film resistance in total, Pa
Δp_{tb}	—	Resistance of airflow across the tube bundle, Pa
Δp_{col}	—	Resistance of airflow across the tube columns, Pa
q	—	Heat flux of rods, kw/m^2
x	—	Air fraction in tube bundle

Greek

Γ	—	Water spray density, kg/(m s)
μ_g	—	Air viscosity, Pa s
μ_l	—	Water viscosity, Pa s
ρ_g	—	Air density, kg/m^3
ρ_l	—	Air density, kg/m^3

Subscripts

act	—	Actual value
col	—	Tube columns
l	—	Liquid phase
g	—	Gas phase
sum	—	In total
tb	—	Tube bundle

Acknowledgments

This work was supported by Shenhua Guohua (Beijing) Electric Power Research Institute Co., Ltd. Project No. 20161048 recorded in Xi'an Jiaotong University.

References

[1] A.T. Wolf, Water and human security, J. Contemp. Water Res. Educ., 118 (2001) 29–37.
[2] C.P. Khedun, R.S. Flores, H. Rughoonundun, R.A. Kaiser, World water supply and use: challenges for the future, Encycl. Agric. Food Syst., 5 (2014) 450–465, doi: 10.1016/B978-0-444-52512-3.00083-8.
[3] A. Ophir, A. Gendel, G. Kronenberg, The LT-MED process for SW Cogen plants, Desal. Water Reuse, 4 (1994) 28–31.
[4] H. Liu, S.Q. Shen, L.Y. Gong, S. Chen, Shell-side two-phase pressure drop and evaporation temperature drop on falling film evaporation in a rotated square bundle, Appl. Thermal Eng., 69 (2014) 214–220.
[5] A. Ophir, F. Lokiec, Advanced MED process for most economical sea water desalination, Desalination, 182 (2005) 187–198.
[6] Y. Xue, X. Du, Z. Ge, L. Yang, Study on multi-effect distillation of seawater with low-grade heat utilization of thermal power generating unit, Appl. Thermal Eng., 141 (2018) 589–599.
[7] A. Al-Othman, N.N. Darwish, M. Qasim, M. Tawalbeh, N.A. Darwish, N. Hilal, Nuclear desalination: a state-of-the-art review, Desalination, 457 (2019) 39–61.
[8] J. Leblanc, J. Andrews, Low-Temperature Multi-Effect Evaporation Desalination Systems Coupled with Salinity-Gradient Solar Ponds, Proceedings of ISES World Congress, Berlin, Heidelberg, 2008, pp. 2151–2157.
[9] N. Shekarchi, F. Shahnia, A comprehensive review of solar-driven desalination technologies 9for off-grid greenhouses, Int. J. Energy Res., 43 (2019) 1357–1386.
[10] G. Venkatesan, S. Iniyan, R. Goic, A prototype flash cooling desalination system using cooling water effluents, Int. J. Energy Res., 37 (2013) 1132–1140.
[11] M. Luqman, I. Ghiat, M. Maroof, F.Z. Lahlou, Y. Bicer, T. Al-Ansari, Application of the concept of a renewable energy based-polygeneration system for sustainable thermal desalination process-a thermodynamics' perspective, Int. J. Energy Res., 44 (2020) 12344–12362.
[12] A.A. Zhukauskas, Convective Transfer in Heat Exchangers, Science Press, Moscow, 1982.
[13] M. Ishak, T.A. Tahseen, M.M. Rahman, Experimental investigation on heat transfer and pressure drop characteristics of air flow over a staggered flat tube bank in crossflow, Int. J. Automot. Mech. Eng., 7 (2013) 900–911.
[14] R.W. Lockhart, R.C. Martinelli, Proposed correlation of data for isothermal two-phase, two-component flow in pipes, Chem. Eng. Prog., 45 (1949) 39–48.
[15] D. Chisholm, A theoretical basis for the Lockhart-Martinelli correlation for two-phase flow, Int. J. Heat Mass Transfer, 10 (1967) 1767–1778.
[16] D.S. Schrage, J.T. Hsu, M.K. Jensen, Two-phase pressure drop in vertical crossflow across a horizontal tube bundle, AIChE J., 34 (1988) 107–115.
[17] R. Dowlati, M. Kawaji, A.M.C. Chan, Pitch-to-diameter effect on two-phase flow across an in-line tube bundle, AIChE J., 36 (1990) 765–772.
[18] G.P. Xu, K.W. Tou, C.P. Tso, Two-phase void fraction and pressure drop in horizontal crossflow across a tube bundle, J. Fluids Eng., 120 (1998) 140–145.
[19] P.A. Feenstra, D.S. Weaver, R.L. Judd, An improved void fraction model for two-phase cross-flow in horizontal tube bundles, Int. J. Multiphase Flow, 26 (2000) 1851–1873.
[20] L. Consolini, D. Robinson, J.R. Thome, Void fraction and two-phase pressure drops for evaporating flow over horizontal tube bundles, Heat Transfer Eng., 27 (2006) 5–21.
[21] J. Mitrovic, Influence of Tube Spacing and Flow Rate on Heat Transfer from a Horizontal Tube to a Falling Liquid Film, International Heat Transfer Conference Digital Library, Begel House Inc., 1986.
[22] X. Hu, A.M. Jacobi, The intertube falling film: part 1-flow characteristics, mode transitions, and hysteresis, J. Heat Transfer, 118 (1996) 616–625.
[23] I.D.R. Grant, D. Chisholm, Two-phase flow on the shell-side of a segmentally baffled shell-and-tube heat exchanger, J. Heat Transfer, 101 (1979) 38–42.
[24] R. Ulbrich, D. Mewes, Vertical, upward gas-liquid two-phase flow across a tube bundle, Int. J. Multiphase Flow, 20 (1994) 249–272.
[25] G.P. Xu, C.P. Tso, K.W. Tou, Hydrodynamics of two-phase flow in vertical up and down-flow across a horizontal tube bundle, Int. J. Multiphase Flow, 24 (1998) 1317–1342.
[26] F.T. Kanizawa, G. Ribatski, Two-phase flow patterns across triangular tube bundles for air-water upward flow, Int. J. Multiphase Flow, 80 (2016) 43–56.
[27] K. Mao, T. Hibiki, Flow regime transition criteria for upward two-phase cross-flow in horizontal tube bundles, Appl. Thermal Eng., 112 (2017) 1533–1546.
[28] L. Gong, S. Shen, H. Liu, X. Chen, Three-dimensional heat transfer coefficient distributions in a large horizontal-tube falling film evaporator, Desalination, 357 (2015) 104–116.
[29] H. Hou, Q. Bi, H. Ma, G. Wu, Distribution characteristics of falling film thickness around a horizontal tube, Desalination, 285 (2012) 393–398.
[30] H. Blasius, Das Aehnlichkeitsgesetz Bei Reibungsvorgangen in Flüssigkeiten, V.d. Ingenieure, Mitteilungen Über Forschungsarbeiten auf Dem Gebiete des Ingenieurwesens, Vol. 131, Springer, Berlin, Heidelberg, 1913, pp. 1–41.
[31] H. Schlichting, Boundary Layer Theory, Mcgraw-Hill Book Co., New York, NY, 1968.
[32] J.W. Palen, G. Breber, J. Taborek, Prediction of flow regimes in horizontal tube-side condensation, Heat Transfer Eng., 1 (1979) 47–57.